Synthesis, structural distortion, and magnetic property of complex perovskites $A\mathrm{Mn}_{0.2}M_{0.8}\mathrm{O}_{2.6}\mathrm{N}_{0.4}$ (A = Sr, Ba; M = Nb, Ta)

Young-Il Kim,[a,*] and Maxim Avdeev[b,c]

[a] *Department of Chemistry, Yeungnam University, Gyeongsan 38541, Republic of Korea*
[b] *Australian Nuclear Science and Technology Organisation, New Illawarra Rd, Lucas Heights, NSW 2234, Australia*
[c] *School of Chemistry, The University of Sydney, Sydney, NSW 2006, Australia*

[*] Corresponding author. E-mail address: yikim@ynu.ac.kr (Y.-I. Kim).

Abstract: Oxynitride complex perovskites, $\mathrm{BaMn}_{0.2}M_{0.8}\mathrm{O}_{2.6}\mathrm{N}_{0.4}$ (M = Nb, Ta), were prepared by reacting the layered oxides $\mathrm{Ba}_5M_4\mathrm{O}_{15}$ with MnCl_2, in the NH_3 atmosphere. Both $\mathrm{BaMn}_{0.2}M_{0.8}\mathrm{O}_{2.6}\mathrm{N}_{0.4}$ phases crystallized in orthorhombic symmetries, in contrast with previous Ba-based perovskite oxynitrides, $\mathrm{Ba}M\mathrm{O}_2\mathrm{N}$ and $\mathrm{Ba}M'_{0.2}M_{0.8}\mathrm{O}_{3-x}\mathrm{N}_x$ (M' = Li, Na, Mg; M = Nb, Ta), all of which were cubic. The thermogravimetry (TG) and differential scanning calorimetry (DSC) of $A\mathrm{Mn}_{0.2}M_{0.8}\mathrm{O}_{2.6}\mathrm{N}_{0.4}$ (A = Sr, Ba; M = Nb, Ta) suggested that the phase stability is higher for A = Ba and M = Ta than for A = Sr and M = Nb, respectively. Both $\mathrm{BaMn}_{0.2}\mathrm{Nb}_{0.8}\mathrm{O}_{2.6}\mathrm{N}_{0.4}$ and $\mathrm{BaMn}_{0.2}\mathrm{Ta}_{0.8}\mathrm{O}_{2.6}\mathrm{N}_{0.4}$ exhibited paramagnetic behavior with effective magnetic moments of 5.75 μ_B and 5.90 μ_B, respectively, well consistent with the high-spin Mn^{2+} state. All the four members of $A\mathrm{Mn}_{0.2}M_{0.8}\mathrm{O}_{2.6}\mathrm{N}_{0.4}$ had negative Weiss constants (θ_W's), indicative of the antiferromagnetic interactions. The variations of the θ_W among $A\mathrm{Mn}_{0.2}M_{0.8}\mathrm{O}_{2.6}\mathrm{N}_{0.4}$ were attributable to the differences in the Mn–O bond lengths (A = Sr vs. Ba) or to the distinct lattice covalency (M = Nb vs. Ta).

1. Introduction

Perovskite oxynitrides have received considerable attention recently, owing to the potential applicability in diverse areas such as visible-light photocatalysts,[1–5] dielectrics,[6–9] pigments,[10–12] and magnetoresistors.[13,14] The material functions of the oxynitrides depend on various factors such as crystal structure and N/O ratio, but the cation composition makes the foremost effects. In an attempt to explore new compositions of the oxynitride perovskites and potentially exotic properties, we have synthesized a group of complex perovskite oxynitrides, $A\mathrm{Li}_{0.2}M_{0.8}\mathrm{O}_{2.8}\mathrm{N}_{0.2}$, $A\mathrm{Na}_{0.2}M_{0.8}\mathrm{O}_{2.8}\mathrm{N}_{0.2}$, and $A\mathrm{Mg}_{0.2}M_{0.8}\mathrm{O}_{2.6}\mathrm{N}_{0.4}$,[15–17] *via* the intercalative route utilizing the layered oxide $A_5M_4\mathrm{O}_{15}$ (A = Sr, Ba; M = Nb, Ta). In terms of composition, the above $AM'_{0.2}M_{0.8}\mathrm{O}_{3-x}\mathrm{N}_x$ (M' = Li, Na, Mg) make unusual cases where low-valence cations are stabilized on the octahedral site of the oxynitride perovskite. These new phases served to reveal a few noteworthy points. First, the N/O ratio is an effective parameter for tuning the optical band gap of oxynitride semiconductors: The band gap widens systematically as the N/O ratio decreases. Moreover, the lower N/O ratio tends to suppress the sub-gap absorptions which are often linked to lattice defects or reduced impurities. Second, the minority species (N^{3-}) of the anion sub-lattice showed a preference for a specific site, in cases multiple anion sites are available.

Recently, we prepared $\mathrm{SrMn}_{0.2}M_{0.8}\mathrm{O}_{2.6}\mathrm{N}_{0.4}$ (M = Nb, Ta) by applying the above intercalative synthetic strategy.[18] Notably, these Mn^{2+}-containing perovskites had an orthorhombic symmetry, contrasting with the whole members of $\mathrm{Sr}M\mathrm{O}_2\mathrm{N}$ and $\mathrm{Sr}M'_{0.2}M_{0.8}\mathrm{O}_{3-x}\mathrm{N}_x$ (M = Nb, Ta; M' = Li, Na, Mg) which are all tetragonal. Such a symmetry-lowering was attributed to the covalency factor contributed from Mn^{2+}. In addition, $\mathrm{SrMn}_{0.2}M_{0.8}\mathrm{O}_{2.6}\mathrm{N}_{0.4}$ (M = Nb, Ta) exhibited paramagnetic behaviors with weak antiferromagnetic interaction resulting from the moderately dilute and randomly distributed Mn^{2+} ions.

In this study, we further prepared the $\mathrm{BaMn}_{0.2}M_{0.8}\mathrm{O}_{2.6}\mathrm{N}_{0.4}$ (M = Nb, Ta) phases and characterized by synchrotron X-ray and neutron powder diffraction, diffuse-reflectance spectroscopy, thermal analysis, X-ray photoelectron spectroscopy, and magnetization measurements. The crystal symmetry, thermochemistry, band gap, and magnetic behaviors of $A\mathrm{Mn}_{0.2}M_{0.8}\mathrm{O}_{2.6}\mathrm{N}_{0.4}$ (A = Sr, Ba; M = Nb, Ta) are presented focusing on the distinctions arising from the type of A and M cations.

2. Experimental

Precursor oxides $A_5M_4O_{15}$ (A = Sr, Nb; M = Nb, Ta) were prepared by a high-temperature ceramic route, using $SrCO_3$ (Sigma Aldrich, 99.9%), $BaCO_3$ (Alfa Aesar, 99.95%), Nb_2O_5 (Alfa Aesar, 99.9985%), and Ta_2O_5 (Kojundo, 99.9%). Synthesis of complex perovskites $SrMn_{0.2}M_{0.8}O_{2.6}N_{0.4}$ (M = Nb, Ta) was described in a previous report.[18] For synthesizing the Ba analogues, $Ba_5M_4O_{15}$ was reacted with $MnCl_2$ (Alfa Aesar, 99.7%) in a similar manner to those employed in the synthesis of $SrMn_{0.2}M_{0.8}O_{2.6}N_{0.4}$. $Ba_5M_4O_{15}$ and $MnCl_2$ (dried overnight at 373 K under 5 Torr, before use) were mixed in a ratio of Mn:M = 1.02:4 using an agate mortar and pestle, pressed to a pellet, and heated in an NH_3 flow (≈100 sccm). The ammonolytic heating cycle consisted of a ramp (10 K/min) from ambient to a designated temperature (T_{am}), dwell for 12 h, and a heater-off cooling to room temperature. The ammonia flow was maintained throughout the entire heat treatment. After examining the progress of phase formation by powder X-ray diffraction (XRD; Rigaku Miniflex600), the ammonolysis was repeated with gradual elevations of T_{am} until a pure phase was obtained.

Finally obtained $BaMn_{0.2}M_{0.8}O_{2.6}N_{0.4}$ samples were subjected to the synchrotron XRD and neutron diffraction (ND). Synchrotron XRD was measured in the high-resolution powder diffractometer at the beamline 9B of Pohang Accelerator Laboratory, Korea. Data were collected in Bragg-Brentano mode using the radiation with λ = 1.5175 Å. ND patterns were obtained using the powder diffractometer Echidna at the OPAL facility[19] of the Australian Nuclear Science Technology Organisation. Data were recorded using a powder sample packed in a vanadium can, with $\lambda \approx$ 1.62 Å over a 2θ range of 10−165°. The synchrotron XRD and ND data were analyzed by Rietveld refinement using the software suite GSAS-EXPGUI.[20,21]

The chemical compositions were analyzed by inductively coupled plasma atomic emission spectroscopy (ICP-AES; Jobin-Yvon, 138 Ultrace, operated at the Ochang Center, Korea Basic Science Institute) and combustion analysis (CE Instruments, Flash EA 1112, operated at the Seoul Center, Korea Basic Science Institute) as well as the Rietveld refinement of the atomic occupancies. The thermogravimetry (TG) and differential scanning calorimetry (DSC) profiles were recorded in a simultaneous thermal analysis system (Setaram, LABSYS evo). Approximately 10 mg of finely ground sample were packed in an alumina cup, and the temperature was raised from 300 to 1673 K at a rate of 10 K/min, in air.

The absorption behavior of $BaMn_{0.2}M_{0.8}O_{2.6}N_{0.4}$ was measured in the ultraviolet-visible-near infrared (UV-Vis-NIR) range using a diffuse-reflectance spectrometer (Agilent, Cary

5000, operated at Core Research Support Center for Natural Products and Medical Materials, Yeungnam University). The measured reflectance (R) was converted to pseudo-absorbance (A) according to Kubelka-Munk function, $A = (1 - R)^2/2R$.[22] The band gap was estimated by constructing the Tauc plots.[23,24] X-ray photoelectron spectroscopy (XPS; Thermo Scientific, K-Alpha) was performed using an Al K_α source (1486.6 eV). The signal intensity was recorded at an interval of 0.1 eV, and each spectrum was acquired by averaging the results of 20 scans. The XPS binding energy was calibrated with the C 1*s* line at 284.6 eV from the adventitious carbon. Magnetic susceptibility was measured using a Quantum Design Physical Properties Measurement System (PPMS) with a vibrating sample magnetometer (VSM) probe from 2.5 to 300 K in an applied magnetic field (H) of 500 Oe under both zero field-cooled and field-cooled conditions. For AMn$_{0.2}$Nb$_{0.8}$O$_{2.6}$N$_{0.4}$ (A = Sr, Ba), field-dependent magnetization was measured at 5 K over the range -90 kOe $\leq H \leq$ 90 kOe.

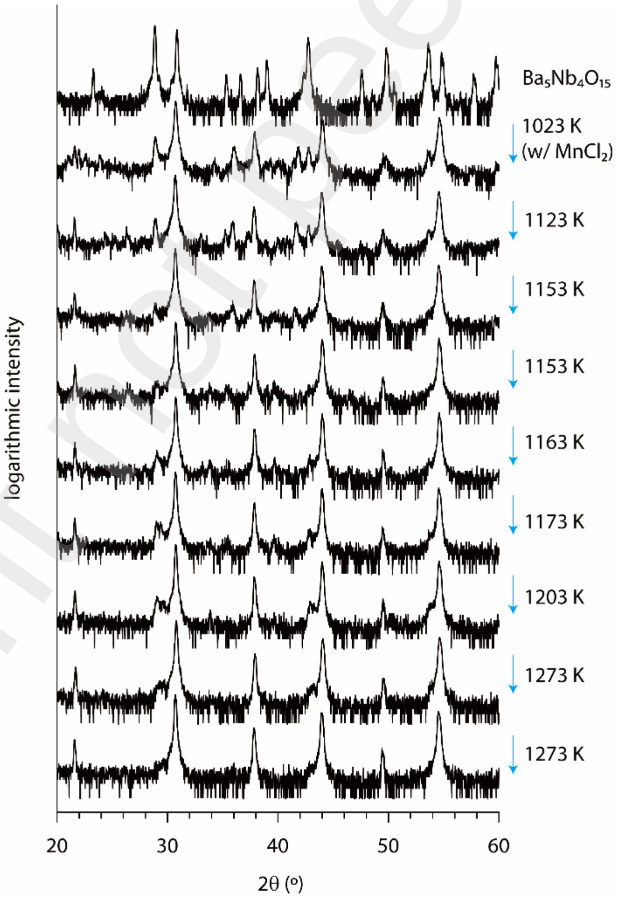

Fig. 1. Progressive evolutions of XRD patterns along the cumulated ammonolytic heating for preparing BaMn$_{0.2}$Nb$_{0.8}$O$_{2.6}$N$_{0.4}$. In all steps, the ammonolysis time was 12 h.

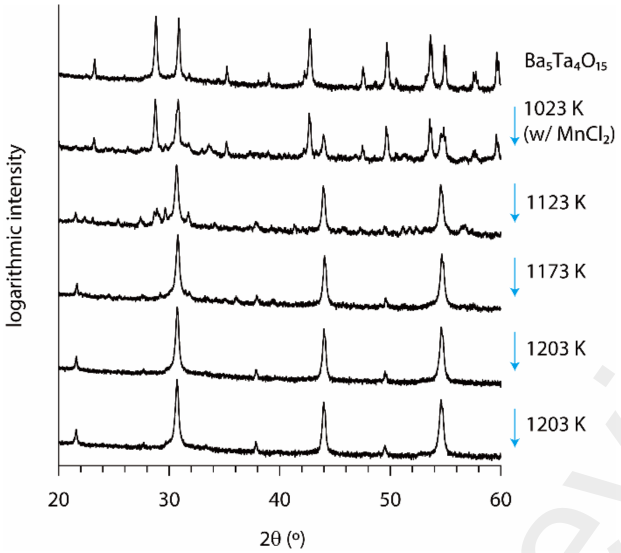

Fig. 2. Progressive evolutions of XRD patterns along the cumulated ammonolytic heating for preparing $BaMn_{0.2}Ta_{0.8}O_{2.6}N_{0.4}$. In all steps, the ammonolysis time was 12 h.

3. Results and Discussion

3.1 Phase formation

Fig. 1 and Fig. 2 show the progressive XRD patterns recorded in the courses of obtaining single-phase samples of $BaMn_{0.2}Nb_{0.8}O_{2.6}N_{0.4}$ and $BaMn_{0.2}Ta_{0.8}O_{2.6}N_{0.4}$, respectively. In both cases, the layered oxide $Ba_5M_4O_{15}$ transformed directly to the 3-dimensional lattice, without significant intermediate phases. The sequential T_{am} profiles had to be delicately controlled to achieve a satisfactory phase purity. Frequently, the complex perovskites, $BaMn_{1/3}M_{2/3}O_3$ (M = Nb, Ta)[25–28] occurred as a stable secondary phase. These ‘3:1:2’ compositions are richer in Mn compared with the target ratio Ba:Mn:M = 5:1:4, and consequently accompanied the formation of $BaCl_2$. However, such a complication had not been encountered in the synthesis of $SrMn_{0.2}M_{0.8}O_{2.6}N_{0.4}$ because the occurrence of $SrMn_{1/3}M_{2/3}O_3$ was insignificant. As for the type of M, the syntheses of $SrMn_{0.2}Nb_{0.8}O_{2.6}N_{0.4}$ and $BaMn_{0.2}Nb_{0.8}O_{2.6}N_{0.4}$ suffered occasional formations of reduced oxynitrides such as NbO_xN_y ($x + y < 1$).

3.2 UV-Vis-NIR and XPS

Fig. 3 shows the Tauc plots of $BaMn_{0.2}M_{0.8}O_{2.6}N_{0.4}$ and $SrMn_{0.2}M_{0.8}O_{2.6}N_{0.4}$ together with photograph images of polycrystalline samples. The direct ($E_{g,\text{ dir}}$) and indirect ($E_{g,\text{ indir}}$) band gaps were estimated as given in Table 1. In accordance with the general trends in the oxide-to-oxynitride conversion, the band gaps of $AMn_{0.2}M_{0.8}O_{2.6}N_{0.4}$ were smaller than those of $A_5M_4O_{15}$ by 1.5~2 eV. Also, the band gap was smaller when M = Nb than when M = Ta. Above results are mainly due to the relative energy levels of the frontier atomic orbitals, N 2p

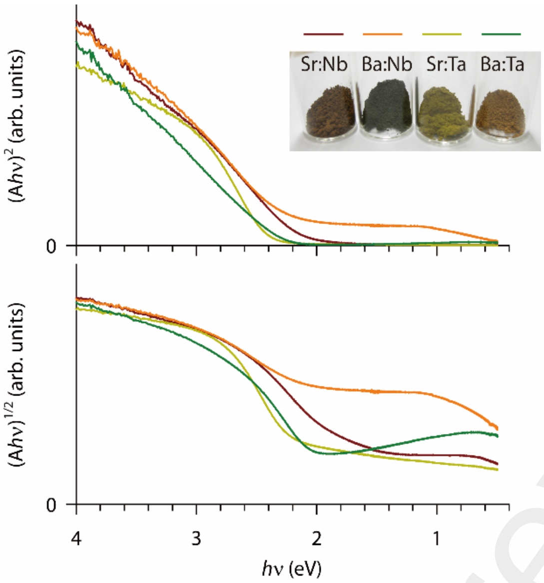

Fig. 3. Photograph images and Tauc plots derived from the diffuse-reflectance spectra for $SrMn_{0.2}Nb_{0.8}O_{2.6}N_{0.4}$ (Sr:Nb), $BaMn_{0.2}Nb_{0.8}O_{2.6}N_{0.4}$ (Ba:Nb), $SrMn_{0.2}Ta_{0.8}O_{2.6}N_{0.4}$ (Sr:Ta), and $BaMn_{0.2}Ta_{0.8}O_{2.6}N_{0.4}$ (Ba:Ta).

> O 2*p* and Nb 4*d* < Ta 5*d*, which directly govern the positions of valence band and conduction band, respectively.[29,30] The effect of *A* cation is less straightforward. The compositions with *A* = Ba, compared with *A* = Sr, tend to have longer *M*–O/N distances and less distorted *M*–O/N–*M* bond angles, leading to a smaller band gap. $BaMn_{0.2}Nb_{0.8}O_{2.6}N_{0.4}$ was found to have non-negligible absorptions in the near infrared region, unlike the other three. Such a sub-gap transition implies the presence of carrier species that were possibly originated from the partial reduction of Nb^{5+}.

Table 1. Band gaps of $AMn_{0.2}M_{0.8}O_{2.6}N_{0.4}$

Composition	$E_{g,\ dir}$ (eV)	$E_{g,\ indir}$ (eV)
$SrMn_{0.2}Nb_{0.8}O_{2.6}N_{0.4}$	2.2	1.4
$SrMn_{0.2}Ta_{0.8}O_{2.6}N_{0.4}$	2.4	2.0
$BaMn_{0.2}Nb_{0.8}O_{2.6}N_{0.4}$	2.1	0.8
$BaMn_{0.2}Ta_{0.8}O_{2.6}N_{0.4}$	2.2	1.8

In this regard, the Nb 3*d* XPS of $SrMn_{0.2}Nb_{0.8}O_{2.6}N_{0.4}$ and $BaMn_{0.2}Nb_{0.8}O_{2.6}N_{0.4}$ was examined to probe the chemical state of niobium (Fig. S2). The Nb 3*d* line of $SrMn_{0.2}Nb_{0.8}O_{2.6}N_{0.4}$ consisted of symmetric $3d_{3/2}$ and $3d_{5/2}$ peaks, representing the presence of single component, Nb^{5+}. On the other hand, the spectrum of $BaMn_{0.2}Nb_{0.8}O_{2.6}N_{0.4}$

displayed an additional component on the lower energy side, and was found to contain Nb^{4+} and Nb^{5+} in a ratio of 87:13 from the line decomposition analysis (Fig. S2). The actual Nb^{4+} fraction in bulk $BaMn_{0.2}Nb_{0.8}O_{2.6}N_{0.4}$ is, however, expected to be lower than 13%, considering the surface-sensitive nature of the XPS technique. Meanwhile, for both $SrMn_{0.2}Ta_{0.8}O_{2.6}N_{0.4}$ and $BaMn_{0.2}Ta_{0.8}O_{2.6}N_{0.4}$, the Ta 4*f* XPS corresponded to the Ta^{5+} states. Indeed, it is well known that Nb is more prone to reduction than Ta. Comparing between $SrMn_{0.2}Nb_{0.8}O_{2.6}N_{0.4}$ and $BaMn_{0.2}Nb_{0.8}O_{2.6}N_{0.4}$, we speculate that the ionic radius of *A*-cation (Sr^{2+}: 1.44 Å, Ba^{2+}: 1.61 Å) played a role in making the difference. That is, $BaMn_{0.2}Nb_{0.8}O_{2.6}N_{0.4}$ has the greater lattice volume, and hence the octahedral volume, than the $SrMn_{0.2}Nb_{0.8}O_{2.6}N_{0.4}$, which will favor the reduction of Nb^{5+} (0.64 Å) to Nb^{4+} (0.68 Å)

3.3 Thermal analysis

Fig. 4 shows the TG-DSC profiles for $AMn_{0.2}M_{0.8}O_{2.6}N_{0.4}$ (A = Sr, Ba; M = Nb, Ta) acquired in air. The mass gain in the intermediate temperature range (800–1050 K for A = Ba, and 700–850 K for A = Sr) and the subsequent mass loss are typical behavior of oxynitride

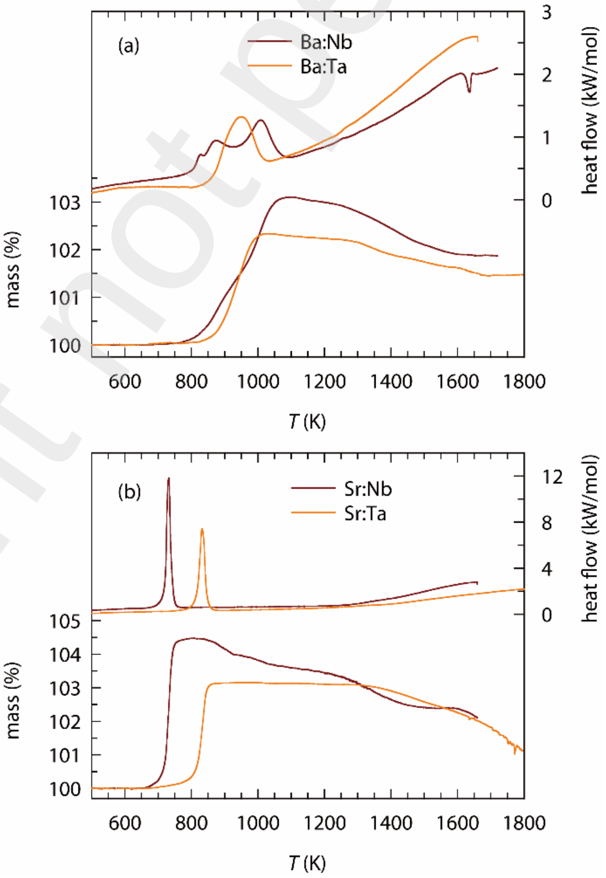

Fig. 4. TG-DSC curves of (a) $BaMn_{0.2}Nb_{0.8}O_{2.6}N_{0.4}$ (Ba:Nb) and $BaMn_{0.2}Ta_{0.8}O_{2.6}N_{0.4}$ (Ba:Ta), and (b) $SrMn_{0.2}Nb_{0.8}O_{2.6}N_{0.4}$ (Sr:Nb) and $SrMn_{0.2}Ta_{0.8}O_{2.6}N_{0.4}$ (Sr:Ta), recorded in air at a rate of 10 K/min.

compounds, and are attributed to the O_2-uptake and N_2-release, respectively.[31–33] The onset temperature of mass gain reflects the phase stability, and increased in the order of $SrMn_{0.2}Nb_{0.8}O_{2.6}N_{0.4}$ < $SrMn_{0.2}Ta_{0.8}O_{2.6}N_{0.4}$ ≈ $BaMn_{0.2}Nb_{0.8}O_{2.6}N_{0.}$ < $BaMn_{0.2}Ta_{0.8}O_{2.6}N_{0.4}$. At the highest temperature part of the TG, the oxynitride sample can be completely converted to a stable oxide phase, thus informing of the N content. $BaMn_{0.2}Nb_{0.8}O_{2.6}N_{0.4}$, $BaMn_{0.2}Ta_{0.8}O_{2.6}N_{0.4}$, and $SrMn_{0.2}Nb_{0.8}O_{2.6}N_{0.4}$ entered a plateau at 1500~1700 K, with the residual masses of ≈101.9 %, ≈101.5 %, and ≈102.5 %, respectively. These values agree with the conversion from $AMn_{0.2}M_{0.8}O_{2.6}N_{0.4}$ to "$AMn_{0.2}M_{0.8}O_{3.3}$", which should involve the replacement of 2N by 3O together with the oxidation of Mn^{2+} to Mn^{3+}. The expected residual masses for the above conversion are 102.1 % ($BaMn_{0.2}Nb_{0.8}O_{2.6}N_{0.4}$), 101.6 % ($BaMn_{0.2}Ta_{0.8}O_{2.6}N_{0.4}$), and 102.5 % ($SrMn_{0.2}Nb_{0.8}O_{2.6}N_{0.4}$). In case of $SrMn_{0.2}Ta_{0.8}O_{2.6}N_{0.4}$, a similar conversion will result in a residual mass of 101.9 %, but a clear plateau was not observed, probably due to subsequent decompositions. The combustion and ICP-AES analyses were employed to investigate the N content and cation ratios, respectively. In all four cases, the N content and A:Mn:M ratio agreed with the respective nominal formula of $AMn_{0.2}M_{0.8}O_{2.6}N_{0.4}$ within two estimated standard deviations. Thus, the thermal events during the above TG-DSC analysis can be divided into sequential parts I and II, represented below:

$$\text{I:}\quad AMn^{2+}{}_{0.2}M_{0.8}O_{2.6}N_{0.4}(s) \rightarrow AMn^{2+}{}_{0.2}M_{0.8}O_{3.2}(N_2)_{0.2}(s)$$

$$\text{II:}\quad AMn^{2+}{}_{0.2}M_{0.8}O_{3.2}(N_2)_{0.2}(s) \rightarrow AMn^{3+}{}_{0.2}M_{0.8}O_{3.3}(s) + 0.2N_2(g)$$

The DSC showed that part I was an exothermic process, where its temperature span agreed roughly with that of mass increase in the respective TG curve. Part I was completed more quickly for A = Sr than for A = Ba. Particularly for $BaMn_{0.2}Ta_{0.8}O_{2.6}N_{0.4}$, part I proceeded through multiple sub-steps. On the other hand, the DSC signal for the part II was much less pronounced, which accords with the slow and steady fashion of the mass drop.

Table 2. Thermochemical information extracted from the TG-DSC analysis

composition	ΔH_I (kJ/mol)	$T_{on, I}$ (K)
$SrMn_{0.2}Nb_{0.8}O_{2.6}N_{0.4}$	–991	680
$SrMn_{0.2}Ta_{0.8}O_{2.6}N_{0.4}$	–914	775
$BaMn_{0.2}Nb_{0.8}O_{2.6}N_{0.4}$	–686	750
$BaMn_{0.2}Ta_{0.8}O_{2.6}N_{0.4}$	–575	829

Table 2 compares the enthalpy of reaction (ΔH_{I}) and the onset temperature ($T_{\mathrm{on,\,I}}$) of part I, where ΔH_{I} was estimated from the DSC peak area by subtracting the smooth baseline from the raw data (Fig. S1), and applying the relation, 1 J = 1 W·s.[33] It is regarded that the smaller $|\Delta H_{\mathrm{I}}|$ and the higher $T_{\mathrm{on,\,I}}$ correspond to the greater stability of $A\mathrm{Mn}_{0.2}M_{0.8}\mathrm{O}_{2.6}\mathrm{N}_{0.4}$. Therefore, the phase stability is higher for M = Ta and A = Ba than for M = Nb and A = Sr, respectively.

3.4 Rietveld refinement

Crystal structures of $\mathrm{BaMn}_{0.2}M_{0.8}\mathrm{O}_{2.6}\mathrm{N}_{0.4}$ were analyzed by joint Rietveld refinement of the XRD and ND patterns. Previous perovskite oxynitrides showed a clear trend between the crystal symmetry and the size of dodecahedral cation, in a way that the phases containing Ba^{2+} and Sr^{2+} adopted the cubic and tetragonal symmetries, respectively. As the only exceptions so far, $\mathrm{SrMn}_{0.2}\mathrm{Nb}_{0.8}\mathrm{O}_{2.6}\mathrm{N}_{0.4}$ and $\mathrm{SrMn}_{0.2}\mathrm{Ta}_{0.8}\mathrm{O}_{2.6}\mathrm{N}_{0.4}$ exhibited orthorhombic symmetries, which was attributed to the strong covalency contribution from Mn^{2+}.

In this regard, the Rietveld refinement of $\mathrm{BaMn}_{0.2}M_{0.8}\mathrm{O}_{2.6}\mathrm{N}_{0.4}$ was tested using various space group models of $Pm\overline{3}m$ (cubic), $I4/mcm$ (tetragonal), $Pnma$ (orthorhombic), and $P2_1/n$ (monoclinic). The fit qualities were assessed based on the goodness parameters and the graphical inspection as well. For both compositions, the cubic model was quickly discarded by examining the peak splitting patterns of the XRD, and the $Pnma$ model yielded the better results than the others. In case of $\mathrm{BaMn}_{0.2}\mathrm{Nb}_{0.8}\mathrm{O}_{2.6}\mathrm{N}_{0.4}$, the $I4/mcm$ and $Pnma$ models yielded R_{wp} values of 0.0892 and 0.0759, respectively. Lowering symmetry to $P2_1/n$ did not result in any further improvement and thus $Pnma$ was concluded to be the best model. For $\mathrm{BaMn}_{0.2}\mathrm{Ta}_{0.8}\mathrm{O}_{2.6}\mathrm{N}_{0.4}$, the refinements using the $I4/mcm$ and $Pnma$ models converged with R_{wp} values of 0.0767 and 0.0672, respectively, while that using the $P2_1/n$ model diverged. Fig. S3 further shows selected 2θ regions of Rietveld fit profiles that support the choice of $Pnma$ model.

In the *Pnma* model, Ba, Mn/Nb (or Ba/Ta), O1/N1, O2/N2 atoms are located on 4*c*, 4*b*, 4*c*, and 8*d* Wyckoff sites, respectively. Refinement used the variables of scale factor, zero-

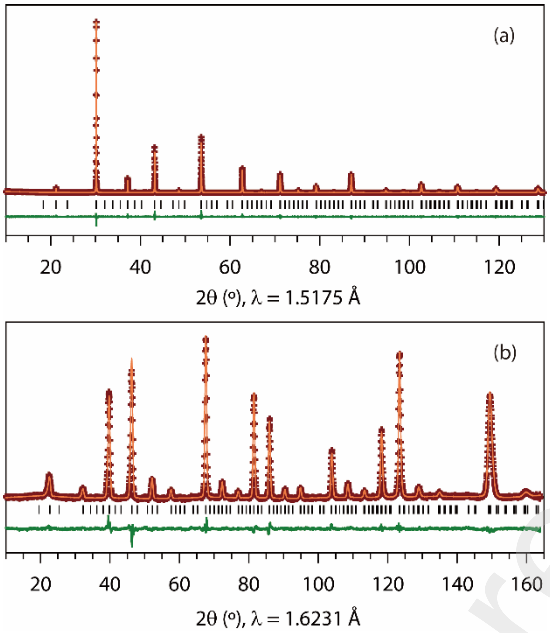

Fig. 5. Joint Rietveld refinement of (a) SXRD and (b) ND patterns for $BaMn_{0.2}Nb_{0.8}O_{2.6}N_{0.4}$ using a *Pnma* model.

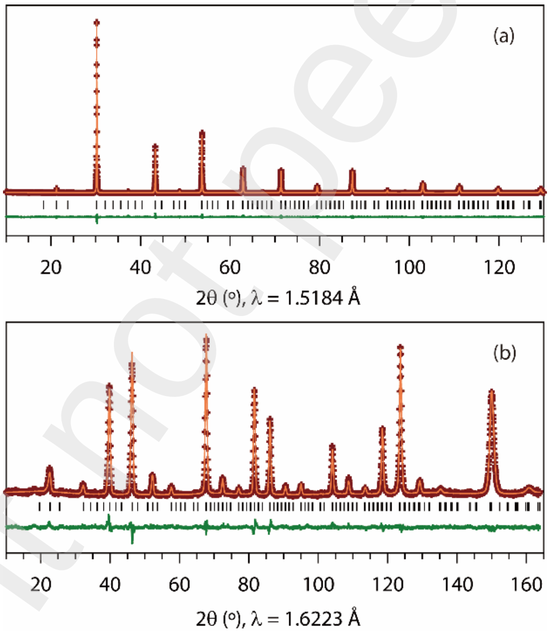

Fig. 6. Joint Rietveld refinement of (a) SXRD and (b) ND patterns for $BaMn_{0.2}Ta_{0.8}O_{2.6}N_{0.4}$ using a *Pnma* model.

point error, fixed background points, peak shape parameters, isotropic temperature factors (U_{iso}), and atomic positions. The occupancies (occ) of Mn/Nb and Mn/Ta were refined but under the constraint of full occupancy of each site, whereas those of O and N were additionally constrained to match the overall anion composition. Fig. 5 and Fig. 6 present the final Rietveld refinement diagrams for $BaMn_{0.2}Nb_{0.8}O_{2.6}N_{0.4}$ and $BaMn_{0.2}Ta_{0.8}O_{2.6}N_{0.4}$, respectively, and Tables 3 and 4 show the refined atomic parameters and selected bond parameters, respectively. As can be noticed from Table 3, the anion occupancies were determined in a semi-constrained manner, for both compounds. When the anion occupancies were refined using the constraints, occ(O1) + occ(N1) = occ(O2) + occ(N2) = 1; occ(O1) + 2 × occ(O1) = 2.6; occ(N1) + 2 × occ(N1) = 0.4, the occ(O1) on the 4*c* site reached as high as 1.1 along with a negative U_{iso}. This was presumably due to the strong correlation between the occupancy and the temperature factor. Note that the coherent neutron scattering lengths of O and N are 5.803 fm and 9.36 fm, respectively,[34] and that the smaller occupancy (overestimation of O/N ratio) can be compensated by the smaller temperature factor. Therefore, test refinements were performed using an additional constraint of U_{iso}(O1/N1) = U_{iso}(O2/N2), in which case, the occ(O1) on the 4*c* site were relatively stable at 1.02~1.03. The anion occupancies were, therefore, judged as occ(O1) = 1, occ(N1) = 0, occ(O2) = 0.8, and occ(N2) = 0.2, for both compositions.

Table 3. Atomic parameters of $BaMn_{0.2}M_{0.8}O_{2.6}N_{0.4}$ (M = Nb, Ta), as determined from joint Rietveld refinement

composition	atom	Site	*x*	*y*	*z*	U_{iso} (Å^2)	occ
M = Nb	Ba	4*c*	0.0020(3)	0.25	0.0006(7)	0.0036(1)	1
	Mn/Nb	4*b*	0.5	0	0	.00060(2)	0.201(2)/0.799
	O1/N1	4*c*	0.490(1)	0.25	0.006(1)	0.0162(8)	1/0
	O2/N2	8*d*	0.253(2)	0.000(2)	0.752(4)	0.0077(3)	0.8/0.2
M = Ta	Ba	4*c*	–0.0014(5)	0.25	0.001(1)	0.0055(1)	1
	Mn/Ta	4*b*	0.5	0	0	0.0062(1)	0.202(2)/0.798
	O1/N1	4*c*	0.512(1)	0.25	0.009(2)	0.0140(4)	1/0
	O2/N2	8*d*	0.251(2)	–0.001(1)	0.755(2)	0.0081(4)	0.8/0.2

$BaMn_{0.2}Nb_{0.8}O_{2.6}N_{0.4}$: Space group *Pnma* ($Z$ = 4); a = 5.82339(4) Å, b = 8.24976(5) Å, c = 5.83275(4) Å, V = 280.214(3) Å^3. R_{wp} = 7.59 %, R_{p} = 5.58 %, χ^2 = 2.07.
$BaMn_{0.2}Ta_{0.8}O_{2.6}N_{0.4}$: Space group *Pnma* ($Z$ = 4); a = 5.81747(5) Å, b = 8.22710(6) Å, c = 5.82518(6) Å, V = 278.798(3) Å^3. R_{wp} = 6.72 %, R_{p} = 4.89 %, χ^2 = 2.09.

Table 4. Selected bond distances (Å) and angles (°) of $BaMn_{0.2}M_{0.8}O_{2.6}N_{0.4}$

	$BaMn_{0.2}Nb_{0.8}O_{2.6}N_{0.4}$	$BaMn_{0.2}Ta_{0.8}O_{2.6}N_{0.4}$
M–*X*1	[2] 2.0636(3)	[2] 2.0585(4)
M–*X*2	[2] 2.041(11)	[2] 2.033(15)
	[2] 2.081(11)	[2] 2.083(15)

M–$X1$–M	[2] 176.2(4)	[2] 175.2(5)
M–$X2$–M	[4] 180.000(2)	[4] 178.8(3)

M represents Mn, Nb, or Ta; and $X1$ and $X2$ represent 4*c* and 8*d* site anions, respectively.

The simple perovskites $\mathrm{Ba}M\mathrm{O_2N}$ (M = Nb, Ta) have a $Pm\bar{3}m$ type unit cell, on the average structural description. By comparison, the structural distortion in $\mathrm{BaMn_{0.2}}M_{0.8}\mathrm{O_{2.6}N_{0.4}}$ can be ascribed to the covalency effect contributed from $\mathrm{Mn^{2+}}$. The presence of Mn, which has considerably lower valence orbital energy than Nb or Ta, can induce pronounced second-order Jahn–Teller (SOJT) structural distortions.[35,36] Indeed, $\mathrm{BaMn_{0.2}}M_{0.8}\mathrm{O_{2.6}N_{0.4}}$ exhibited notable intra-octahedral distortions, as summarized in Table 4. On the other hand, the octahedral tilting distortions[37] in $\mathrm{BaMn_{0.2}}M_{0.8}\mathrm{O_{2.6}N_{0.4}}$ were only minimal as depicted in Fig. 7, probably due to the occupation of the dodecahedral site by a bulky cation $\mathrm{Ba^{2+}}$. Table 5 shows the bond valence sum (BVS)[38] values calculated based on the refined crystal structures. For both compounds, the cationic constituents showed markedly deviated BVS from the ideal valences, reminding that $\mathrm{Ba^{2+}}$ and $\mathrm{Mn^{2+}}$ are larger and $\mathrm{Nb^{5+}}$/$\mathrm{Ta^{5+}}$ are smaller, as compared with the respective void spaces in the $\mathrm{BaMn_{0.2}}M_{0.8}\mathrm{O_{2.6}N_{0.4}}$ lattice. Those deviations of BVS were implausibly large for a stable structure, implying that the local structure of $\mathrm{BaMn_{0.2}}M_{0.8}\mathrm{O_{2.6}N_{0.4}}$ might differ substantially from the average structure. In fact, the non-uniform polyhedral distortions and atomic disorders have prevailed among the perovskite oxynitrides.[39–43] Most notably, the local structure of $\mathrm{BaTaO_2N}$ has been extensively studied for understanding the origin of the unusual dielectric behavior.[39–41]

Table 5. BVS parameters (in valence units) for $\mathrm{BaMn_{0.2}}M_{0.8}\mathrm{O_{2.6}N_{0.4}}$, taking into account the atomic site occupancies

	$\mathrm{BaMn_{0.2}Nb_{0.8}O_{2.6}N_{0.4}}$	$\mathrm{BaMn_{0.2}Ta_{0.8}O_{2.6}N_{0.4}}$
Ba	2.38	2.42
Mn	2.94	2.97
Nb/Ta	4.16	4.29
O(4*c*)	–1.99	–2.04
N(4*c*)	–2.82	–2.86
O(8*d*)	–1.99	–2.04
N(8*d*)	–2.82	–2.85

Bond valence (bv) was calculated from the relation, $bv = \exp\{(R_0 - d_{ij})/0.37\}$, using the R_0 parameters: $\mathrm{Ba^{2+}}$–$\mathrm{O^{2-}}$ 2.285 Å, $\mathrm{Ba^{2+}}$–$\mathrm{N^{3-}}$ 2.47 Å, $\mathrm{Mn^{2+}}$–$\mathrm{O^{2-}}$ 1.790 Å, $\mathrm{Mn^{2+}}$–$\mathrm{N^{3-}}$ 1.84 Å, $\mathrm{Nb^{5+}}$–$\mathrm{O^{2-}}$

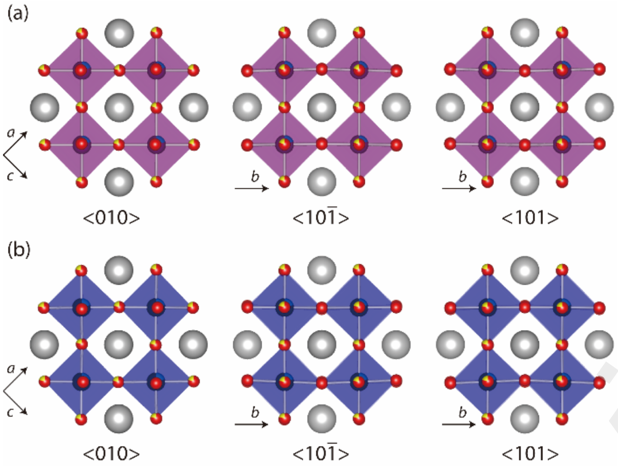

Fig. 7. Octahedral linkages of (a) $BaMn_{0.2}Nb_{0.8}O_{2.6}N_{0.4}$ and (b) $BaMn_{0.2}Ta_{0.8}O_{2.6}N_{0.4}$, viewed along ⟨010⟩, ⟨10$\bar{\mathbf{1}}$⟩, and ⟨101⟩ directions. Sectored spheres at the octahedral corners indicate the partial occupations by O (red) and N (yellow).

1.911 Å, Nb^{5+}–N^{3-} 2.01 Å, Ta^{5+}–O^{2-} 1.920 Å, Ta^{5+}–N^{3-} 2.01 Å.

3.5 Magnetic properties

The temperature (T)-dependent magnetization of $BaMn_{0.2}M_{0.8}O_{2.6}N_{0.4}$ (M = Nb, Ta) was measured from 2.5 to 300 K in an applied field of 500 Oe, where both compounds exhibited paramagnetic behavior, similarly to $SrMn_{0.2}M_{0.8}O_{2.6}N_{0.4}$.[18] The molar susceptibility (χ_m) was fitted based on the Curie-Weiss law, $\chi_m = C/(T - \theta_W)$, in the range of T = 50–300 K. Fig. 8 displays the fitting results of $AMn_{0.2}M_{0.8}O_{2.6}N_{0.4}$ (A = Sr, Ba; M = Nb, Ta), where the line

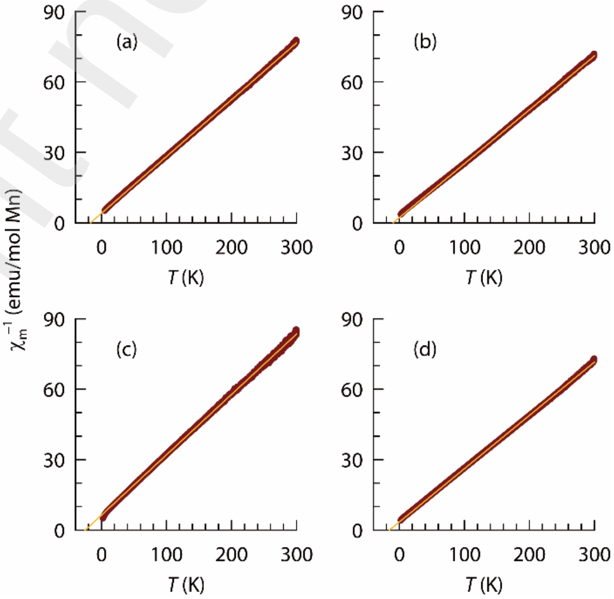

Fig. 8. Curie-Weiss fitting (50–300 K) for the temperature-dependent magnetic susceptibilities of (a) $BaMn_{0.2}Nb_{0.8}O_{2.6}N_{0.4}$, (b) $BaMn_{0.2}Ta_{0.8}O_{2.6}N_{0.4}$, (c) $SrMn_{0.2}Nb_{0.8}O_{2.6}N_{0.4}$, and (d) $SrMn_{0.2}Ta_{0.8}O_{2.6}N_{0.4}$.

slope and the x-intercept informed of the effective magnetic moment (μ_{eff} per Mn) and the Weiss constant (θ_W), respectively. As given in Table 6, all the above four compounds had μ_{eff} values corresponding to the high-spin Mn^{2+} state ($S = 5/2$, theoretical spin-only value of 5.92 μ_B), and negative Weiss constants indicative of the dominance of antiferromagnetic interactions.

Table 6. Magnetic parameters obtained from the fitting of magnetic susceptibility

Composition	μ_{eff} (μ_B) per Mn	θ_W (K)
$SrMn_{0.2}Nb_{0.8}O_{2.6}N_{0.4}$	5.60	−24.7
$SrMn_{0.2}Ta_{0.8}O_{2.6}N_{0.4}$	5.94	−15.4
$BaMn_{0.2}Nb_{0.8}O_{2.6}N_{0.4}$	5.75	−16.8
$BaMn_{0.2}Ta_{0.8}O_{2.6}N_{0.4}$	5.90	−9.7

In the manganese-containing perovskites, Mn^{3+} or Mn^{4+} states are more frequent than the Mn^{2+} state,[44] and the high-spin configurations are favored regardless of the oxidation state. The Mn^{2+} compounds tended to exhibit antiferromagnetic interactions *via* the superexchange mechanism,[25,45] while the Mn^{3+} compounds usually showed ferromagnetic double exchange interactions.[46,47] The magnetic behaviors of $AMn_{0.2}M_{0.8}O_{2.6}N_{0.4}$ are, therefore, consistent with the general trend of the Mn^{2+} compounds. The μ_{eff} values of $AMn_{0.2}M_{0.8}O_{2.6}N_{0.4}$ indicate that the magnetic contributions from M^{5+} ions are negligible, as expected. The θ_W's of $AMn_{0.2}M_{0.8}O_{2.6}N_{0.4}$ are fairly close to 0 K, presumably due to the low concentration and the random distribution of Mn^{2+}. From the comparison of θ_W, it is judged that the superexchange coupling is stronger when A = Sr or M = Nb than when A = Ba or M = Ta, respectively. Previous studies suggested, for the oxide perovskites with magnetic ion B, that the covalent superexchange coupling depends on the bond angle of B–O–B (θ) and the bond length of B–O (d).[48,49] In particular, Goodenough et al.[49] demonstrated that the spin-spin coupling correlates well with an empirical parameter, $\cos^4\{(\pi-\theta)/2\}/d^7$. Using the average values of θ and d, the above parameter (in Å^{-7}) is calculated as ≈0.0063 for both $BaMn_{0.2}M_{0.8}O_{2.6}N_{0.4}$ and ≈0.0068 for both $SrMn_{0.2}M_{0.8}O_{2.6}N_{0.4}$, which accords with the lower θ_W for A = Sr than for A = Ba. Although the type of M made insignificant differences in the structural parameters, it apparently affected the θ_W, implying that $AMn_{0.2}Nb_{0.8}O_{2.6}N_{0.4}$ has more covalent lattice than the respective $AMn_{0.2}Ta_{0.8}O_{2.6}N_{0.4}$.

4. Conclusions

Perovskite oxynitrides $BaMn_{0.2}M_{0.8}O_{2.6}N_{0.4}$ (M = Nb, Ta) were newly synthesized by the intercalative modification of the layered oxides $Ba_5M_4O_{15}$. These two oxynitrides are latest additions to the family of $AM'_{0.2}M_{0.8}O_{3-x}N_x$ (A = Sr, Ba; M' = Li, Na, Mg, Mn; M = Nb, Ta). The joint Rietveld refinement of the synchrotron XRD and ND patterns revealed that $BaMn_{0.2}M_{0.8}O_{2.6}N_{0.4}$ have orthorhombic (*Pnma*) symmetries with moderate intra-octahedral distortions and minute octahedral tilting distortions. The unusual structural distortions of $BaMn_{0.2}M_{0.8}O_{2.6}N_{0.4}$, as compared with other Ba-based perovskite oxynitrides, are similar to the contrast between $SrMn_{0.2}M_{0.8}O_{2.6}N_{0.4}$ and other Sr-based perovskite oxynitrides, and are ascribed to the enhanced covalency contributed from Mn^{2+}. Conforming to the general attribute of oxynitride phases, $AMn_{0.2}M_{0.8}O_{2.6}N_{0.4}$ (A = Sr, Ba; M = Nb, Ta) have limited stabilities in the air and undergo exothermic transformations to oxide intermediates. The TG-DSC analysis indicated that the thermal stability of $AMn_{0.2}M_{0.8}O_{2.6}N_{0.4}$ depended on the composition (A:M), and followed the order, Ba:Ta > Sr:Ta > Ba:Nb > Sr:Nb. The band gaps of $AMn_{0.2}M_{0.8}O_{2.6}N_{0.4}$ were also dependent on the cation composition, and decreased in an order, Sr:Ta > Ba:Ta > Sr:Nb > Ba:Nb, where the type of M played the more important role. All four $AMn_{0.2}M_{0.8}O_{2.6}N_{0.4}$ phases exhibited typical paramagnetic behaviors arising from the randomly distributed dilute Mn^{2+} ions, part of which are involved in superexchange couplings.

Acknowledgements

This work was supported by the National Research Foundation of Korea through Basic Science Research Program (NRF-2015R1D1A1A01056591). We thank Prof. Jong-Sook Lee and Dr. Thuy Linh Pham for the TG and DSC measurements.

References

1 K. Maeda, *Adv. Mater.*, 2019, **31**, 1808205 (38 pages).

2 K. Maeda, M. Higashi, D. Lu, R. Abe and K. Domen, *J. Am. Chem. Soc.*, 2010, **132**, 5858–5868.

3 T. Takata, C. Pan and K. Domen, *Sci. Technol. Adv. Mater.*, 2015, **16**, 033506 (18 pages).

4 Y. Wu, P. Lazic, G. Hautier, K. Persson and G. Ceder, *Energy Environ. Sci.*, 2013, **6**, 157–168.

5 S. G. Ebbinghaus, H.-P. Abicht, R. Dronskowski, T. Muller, A. Reller and A. Weidenkaff, *Prog. Solid State Chem.*, 2009, **37**, 173–205.

6 Y.-I. Kim, P. M. Woodward, K. Z. Baba-Kishi and C. W. Tai, *Chem. Mater.*, 2004, **16**, 1267–1276.

7 Y.-I. Kim, W. Si, P. M. Woodward, E. Shutter, S. Park and T. Vogt, *Chem. Mater.*, 2007, **19**, 618–623.

8 Y. Hinuma, H. Moriwake, Y.-R. Zhang, T. Motohashi, S. Kikkawa, I. Tanaka, *Chem. Mater.*, 2012, **24**, 4343–4349.

9 Y. Masubuchi, F. Kawamura, T. Taniguchi and S. Kikkawa, *J. Eur. Ceram. Soc.*, 2015, **35**, 1191–1197.

10 M. Jansen and H. P. Letschert, *Nature*, 2000, **404**, 980–982.

11 Y.-I. Kim and P. M. Woodward, *J. Solid State Chem.*, 2007, **180**, 3224–3233.

12 Y.-I. Kim, *Ceram. Int.*, 2014, **40**, 5275–5285.

13 M. Yang, J. Oro-Sole, A. Kusmartseva, A. Fuertes and J. P. Attfield, *J. Am. Chem. Soc.*, 2010, **132**, 4822–4829.

14 D. Oka, Y. Hirose, S. Nakao, T. Fukumura and T. Hasegawa, *Commun. Phys.*, 2021, **4**, 269 (8 pages).

15 Y.-I. Kim, Y. Paik and M. Avdeev, *Cryst. Growth Des.*, 2015, **15**, 53–61.

16 K. H. Moon, J.-M. Kim, Y. Sohn, D. W. Cho, Y.-I. Kim and M. Avdeev, *Dalton Trans.*, 2016, **45**, 5614–5621.

17 K. H. Moon, M. Avdeev and Y.-I. Kim, *J. Solid State Chem.*, 2017, **254**, 1–8.

18 Y.-I. Kim and M. Avdeev, *Dalton Trans.*, 2020, **49**, 6471–6477.

19 M. Avdeev and J. R. Hester, *J. Appl. Crystallogr.*, 2018, **51**, 1597–1604.

20 A. C. Larson and R. B. von Dreele, General Structure Analysis System, Los Alamos National Laboratory, Los Alamos, 1994.

21 B. H. Toby, *J. Appl. Crystallogr.*, 2001, **34**, 210–213.

22 P. Kubelka and F. Munk, *Z. Tech. Phys.(Leipzig)*, 1931, **12**, 593–601.

23 J. Tauc, R. Grigorovici and A. Vancu, *phys. stat. sol.*, 1966, **15**, 617–637.

24 J. Tauc, *Mater. Res. Bull.*, 1968, **3**, 37–46.

25 Y. Xin, Q. Huang, Z. Shafieizadeh and H. Zhou, *J. Solid State Chem.*, 2018, **262**, 8–15.

26 Y. Liu, R. L. Withers, A. P. Whichello, L. Noren, V. Ting, F. Brink and J. D. FitzGerald, *J. Solid State Chem.*, 2005, **178**, 3389-3395.

27 U. Treiber and S. Kemmler-Sack, *J. Solid State Chem.*, 1982, **43**, 51–62.

28 M. Lee, E. S. Choi, X. Huang, J. Ma, C. R. Dela Cruz, M. Matsuda, W. Tian, Z. L. Dun, S. Dong and H. D. Zhou, *Phys. Rev. B*, 2014, **90**, 224402 (8 pages).

29 J. B. Mann, T. L. Meek and L. C. Allen, *J. Am. Chem. Soc.*, 2000, **122**, 2780–2783.

30 J. B. Mann, T. L. Meek, E. T. Knight, J. F. Capitani and L. C. Allen, *J. Am. Chem. Soc.*, 2000, **122**, 5132–5137.

31 L. Le Gendre, R. Marchand and Y. Laurent, *J. Eur. Ceram. Soc.*, 1997, **17**, 1813−1818.

32 F. Tessier, L. Le Gendre, F. Chevire, R. Marchand and A. Navrotsky, *Chem. Mater.*, 2005, **17**, 3570–3574.

33 J. W. Seol, Y.-I. Kim, T. L. Pham and J.-S. Lee, *J. Korean Ceram. Soc.*, 2020, **57**, 432–439.

34 V. F. Sears, *Neutron News*, 1992, **3**, 26–37.

35 R. G. Pearson, *Proc. Nat. Acad. Sci. USA*, 1975, **72**, 2104–2106.

36 I. B. Bersuker, *Chem. Rev.*, 2011, **101**, 1067–1114

37 P. M. Woodward, *Acta Crystallogr. B*, 1977, **53**, 32–43.

38 I. D. Brown, *Chem. Rev.*, 2009, **109**, 6858–6919.

39 C. M. Fang, G. A. de Wijs, E. Orhan, G. de With, R. A. de Groot, H. T. Hintzen and R. Marchand, *J. Phys. Chem. Solids*, 2003, **64**, 281–286.

40 B. Ravel, Y.-I. Kim and P. M. Woodward, *Phys. Rev. B*, 2006, **73**, 184121 (7 pages).

41 R. L. Withers, Y. Liu, P. M. Woodward and Y.-I. Kim, *Appl. Phys. Lett.*, 2009, **92**, 102907 (3 pages).

42 S.-M. Paek and Y.-I. Kim, *J. Solid State Chem.*, 2018, **267**, 92–97.

43 X. Wang, B. Jiang, Y. Zhang, Y.-I. Kim and K. Page, *Inorg. Chem.*, 2021, **60**, 14190–14201.

44 J. B. Goodenough, *Rep. Prog. Phys.*, 2004, **67**, 1915–1993.

45 J. B. Goodenough, *Phys. Rev.*, 1955, **100**, 564–573.

46 Y. Moritomo, A. Asamitsu, H. Kuwahara and Y. Tokura, *Nature*, 1996, **380**, 141–144.

47 T. K. Mandal, V. V. Poltavets, M. Croft and M. Greenblatt, J. Solid State Chem., 2008, 181, 2325–2331.

48 D. Trevis, M. Eibschutz and P. Coppens, *Phys. Lett.*, 1965, **17**, 216–217.

49 J.-S. Zhou and J. B. Goodenough, *Phys. Rev. B*, 2008, **77**, 132104 (4 pages).